Simulating Synchrotron Optical Flashes in the Reverse Shock of a Gamma Ray Burst

Connor Bice

Physics Department, Oregon State University

Advisor: Dr Davide Lazzati

2015/16

Abstract

We construct a Monte Carlo simulation in Python to calculate optical flashes at 5×10^{14} Hz peaking at 6×10^{31} erg s^{-1}Hz^{-1}St^{-1} due to synchrotron radiation from the reverse shock of a gamma-ray burst's jet. While analytical solutions to this problem exist, they rely on sweeping simplifications of what is necessarily a highly variable and complex system. The simulation expands upon the well understood properties of single-electron synchrotron to predict observer-frame light curves from isotropic but analytically intractable outflows. The light curves produced compare favorably with theoretical predictions for simpler jets. Unfortunately, the simulation so far fails to resolve features associated with the geometry of our jet. Work continues toward a solution to this problem.

Table of Contents

List of Figures

Chapter 1 - Introduction

1.1 Motivation and Objective

The study of gamma ray bursts (GRBs) has potentially immense scientific value. Not only do they constitute a glamorous and intriguing topic in and of themselves, but GRBs can be extremely useful tools for the study of very distant regions of the universe. Because of their association with massive star formation and extraordinary luminosities, GRBs can act as probes of galaxy evolution in the high-redshift universe, reaching back even as far as reionization (Gehrels, Ramirez-Ruiz, and Fox, 2009). Increasing our understanding of GRBs then has direct and immediate benefits for the field of cosmology.

The onward march of technology has led to an explosion of observations on gamma ray bursts in recent years. Astronomers have finally found strong footing atop ever-growing heaps of data from which to study GRBs, which for years after their discovery were just transient flashes lighting up the gamma sky and disappearing too quickly to trace. This observational surge has provided theorists with all important benchmarks against which to test their models. While many papers have been published which compute light curves from various regions of the burst, few or none so far have predicted the extreme variability which is such a defining characteristic of GRB prompt emissions.

We present in this paper the construction and results of a monte-carlo type simulation for synchrotron emission from the reverse shock of a GRB's outflow. The simulation is capable of producing synchrotron curves from jets with extremely variable hydrodynamic structure. We hope to demonstrate that the variability observed from the prompt optical emission of a GRB is consistent with the prevailing model of synchrotron radiation from the reverse shock. If successful, this work could provide an increased measure of confidence in the reverse shock models for future research, and may also offer insights into the source conditions and structures of observed GRBs.

1.2 Gamma Ray Bursts

Gamma ray bursts are incredibly fascinating phenomena. They are characterized by intense flashes of radiation, peaking in the titular gamma ray band. Although the prompt emission from a GRB resolves on a time scale measured in seconds, it can outshine the rest of the gamma ray sky, the sun included, while active (Gehrels, Ramirez-Ruiz, and Fox, 2009). The first detection of a GRB was on July 2, 1967, by military satellites watching for violations of the Nuclear Test Ban Treaty. For nearly thirty years afterward, however, despite the detection of two to three GRBs daily, their short durations made it impossible for telescopes to make detailed observations. In 1997, telescopes which were able to pinpoint the origins of GRBs were finally in place, and follow-up observations began in earnest. They found that GRBs are distributed isotropically throughout the sky, which is to say that their sources are not, in general, within the Milky Way. Proper appreciation for the distances involved leads to the conclusion that the energy radiated by a GRB can exceed 10^{53} erg, making them the most luminous events in the known universe.

Better observations of GRBs have allowed for the identification of several features in addition to the prompt gamma emission. During that period, a typical GRB produces nearly as much energy in x rays, and in roughly 50% of observed bursts, a flash in the optical band which while still bright, contains energy roughly four orders of magnitude below the gamma emission. While these effects resolve in a matter of seconds, a lingering afterglow is also seen. The afterglow typically appears as a continuation and evolution of the x ray component of the prompt emission, as it slowly fades through optical and radio bands over the course of several weeks. The duration of the afterglow has made observations on it relatively easy, and as a consequence it is much better understood than the prompt emissions.
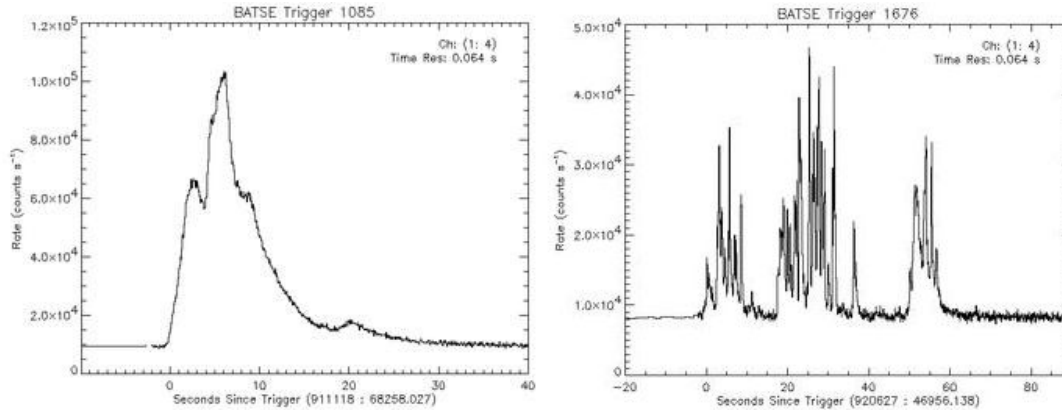
Figure 1.1 The emission from GRBs is highly variable. Here we see two separate bursts detected by the BATSE instrument on board the Compton Gamma Ray Observatory. These curves are for photons with energy >20 keV, which includes hard x rays and extends into the gamma band.

As observations of gamma ray bursts have improved, so too has the theory. GRBs have been shown to be associated with supernovae. While the correlation with stellar death is not ubiquitous, and other models exist, it is still taken to be at the root of many if not all GRBs. In particular, accretion onto a neutron star or stellar mass black hole during a core collapse supernova has been computationally shown to provide the necessary power to drive a GRB. Moreover, the angular momentum associated with such an engine allows it to collimate a jet to tunnel through the infalling stellar material. It is this ultra-relativistic stream of charged particles which is commonly held to be the source of the radiation observed in a GRB, regardless of the engine.

1.3 Shocks

If a wave propagates through a medium faster than the speed of sound, it is referred to as a shock wave. Like any wave, they carry energy, but shock waves are characterized by nearly discontinuous changes in density and pressure. For a fluid flow, this discontinuity comes about from the medium's inability to clear a path, when it instead "piles up" on the shock front. The ultra-relativistic jet ascribed to gamma-ray bursts is accordingly predicted to produce extreme shocks when it interacts with the interstellar medium (Sari and Piran, 1999).

The jet of a gamma-ray burst is expected to produce two shocks. The first travels outward from the burst and is referred to as the forward shock. Typically, the forward shock resolves over several days and is indicated as the source of the burst's x-ray, optical, and radio afterglow. The second shock is the complement to the first, travelling back into the jet, and is

referred to as the reverse shock. The reverse shock can traverse the entire jet in just seconds, and is predicted to induce intense and turbulent magnetic fields in the fireball (Sari and Piran, 1999). For these two reasons, the reverse shock is theorized to be the source of the mysterious optical flashes occasionally observed alongside the prompt gamma-ray emission.

1.4 Synchrotron Radiation

Accelerating charges produce electromagnetic radiation. While there are many mechanisms by which to accelerate charges in the outflow of a gamma-ray burst, this paper focuses on a process known as synchrotron emission. Synchrotron is widely accepted to be the primary source of the radiation attributed to gamma-ray burst outflows (Gehrels, Ramirez-Ruiz, and Fox, 2009).

A theoretical understanding of the synchrotron mechanism can be achieved by first considering cyclotron emission. Charged particles moving within a magnetic field are subject to the Lorentz force, which acts perpendicularly to the charge's motion. For a locally uniform field B, this force results in helical motion with radius

$$r_c = \frac{mv}{qB}$$ **(1.1)**

As the perpendicular velocity v in this motion is constant, it is a simple matter to find the period of the cycle and thus the frequency:

$$\nu_c = \frac{qB}{2\pi m}$$ **(1.2)**

Disregarding the broadening effects of imperfections in the environment, we see that cyclotron emits at only a single frequency. When the velocity of the charged particle with respect to the field enters the relativistic regime, however, the emission becomes more complex. This class of cyclotron radiation is referred to as synchrotron. Two relativistic effects become important when adapting cyclotron to the synchrotron regime. First: the effective mass of the particle is increased by the Lorentz factor γ, so the fundamental frequency is reduced by γ. Perhaps more importantly, beaming (see figure 1.2) introduces time domain periodicity in the observed radiation.

6
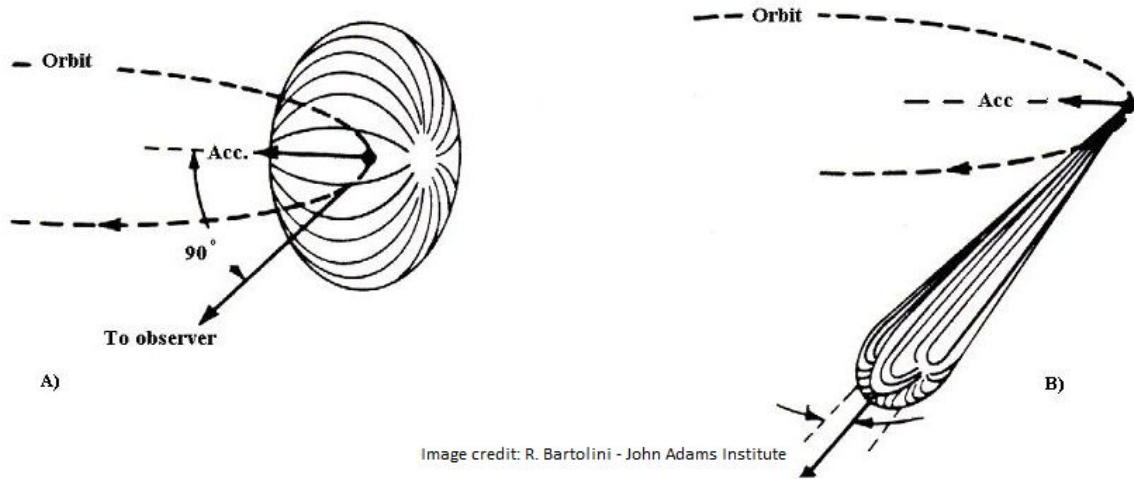
Fig 1.2 A) With cyclotron radiation, the emission is isotropic. The observer sees the same emission regardless of where the particle is in its cycle. B) With synchrotron, however, relativistic beaming strongly collimates the emission into a solid angle of roughly $1/\Gamma$. Consequently, the observer sees very narrow emission in the time domain and a broadened spectrum.

What was once a temporally constant, single frequency emission is changed to be strongly peaked temporally, so a simple Fourier analysis leads to the conclusion that additional frequencies must have been introduced. These additional frequencies are all harmonics of the fundamental, v_c/γ, but approach a continuous spectrum as γ becomes large. In the continuous limit, the synchrotron spectrum is maximal at

$$v_s = \gamma^2 v_c \qquad\qquad (1.3)$$

In spite of the reduced fundamental frequency, synchrotron radiates the bulk of its energy at frequencies much larger than the cyclotron frequency. Thanks to their predictability, cyclotron and synchrotron are essential tools in determining the magnetic fields of distant luminous objects. The shocks associated with relativistic jets, in particular, engender intense magnetic fields and carry an abundance of highly energetic charged particles. As a consequence, they are prime sources of synchrotron radiation.

1.5 Special Relativity

1.5.1 Basics

Einstein's special theory of relativity describes the laws and effects that derive from the acceptance of the speed of light as the ultimate speed limit in the universe, and how they affect transformations between reference frames. In several places so far, we have discussed the Lorentz factor. We now define it:

$$\gamma = \left(1 - \tfrac{v^2}{c^2}\right)^{-1/2} \tag{1.4}$$

The Lorentz factor can be seen as a measure of "how close to the speed of light" a relative velocity is. For $v = 0$, we observe that $\gamma = 1$, and for $v \to c$, the Lorentz factor approaches infinity. While we will present many results with little derivation, the Lorentz factor appears explicitly in many of the frame transformations of special relativity.

For an object with rest length L' moving toward an observer at speed v, the observer measures it to have a length $L \neq L'$. This can be attributed to the fact that the measurement is made using photons which arrived simultaneously, while the extra distance traveled by the photons from the back of the object means they were not emitted simultaneously. Careful analysis leads to the result that

$$L = \sqrt{1 - \tfrac{v^2}{c^2}} L' = \tfrac{L'}{\gamma} \tag{1.5}$$

Because the Lorentz factor is at least 1, the observed length is reduced and this result is referred to as length contraction. This effect resurfaces for any measure involving lengths, with the density being particularly important in this study. Since the orthogonal lengths are unaffected, we find that the volumetric mass density transform is simply

$$\rho = \gamma \rho' \tag{1.6}$$

Through similar arguments, we can see the effects of relativistic motion on duration as well. Again we consider a particle moving toward an observer at velocity v, and look at when photons arrive. Done carefully, we see that if the object performs an action for an amount of time T', then for the observer, the duration of the action is

$$T = \sqrt{\frac{1}{1-v^2/c^2}}\, T' = \gamma T' \qquad\qquad \textbf{(1.7)}$$

Because the observer's duration is always longer than the actor's duration, this effect is known as time dilation.

1.5.2 Beaming

While defining synchrotron radiation, reference was made to an effect called beaming. The effect can be quantified by considering observations of an object moving with velocity *u'* in its own frame (with components $u_\parallel{}'$ and $u_\perp{}'$), while moving with relative velocity *v*. As expressed by Rybicki (1979):

$$u_\parallel = \frac{u_\parallel{}'+v}{1+vu_\parallel{}'/c^2} \;, \quad u_\perp = \frac{u_\perp{}'}{\gamma(1+vu_\parallel{}'/c^2)} \qquad\qquad \textbf{(1.8)}$$

If we allow the velocity *u'* to be the speed of light, and look at the angle of its motion with respect to the relative velocity, then we see that

$$tan(\theta) = \frac{sin(\theta')}{\gamma(cos(\theta')+v/c)} \;, \quad cos(\theta) = \frac{cos(\theta')+v/c}{1+(v/c)cos(\theta')} \qquad\qquad \textbf{(1.9)}$$

Finally, we examine the result for the case that $\theta' = \frac{\pi}{2}$. Applied to the idea of isotropic emission, this is the boundary for all radiation in the "forward facing" hemisphere. In the observer frame, this becomes

$$tan(\theta) = \frac{c}{\gamma v} \;, \quad cos(\theta) = \frac{v}{c} \; \rightarrow \; sin(\theta) = \frac{1}{\gamma} \qquad\qquad \textbf{(1.10)}$$

and it becomes obvious that in the limit of very relativistic particles (large γ),

$$\theta \approx \frac{1}{\gamma} \qquad\qquad \textbf{(1.11)}$$

This is the exact result cited as beaming in the previous section. The introduction of a significant relative velocity between emitter and observer causes an isotropic emission to collimate half of its total radiation into a cone of solid angle $1/\gamma$, while almost fully evacuating the backward directions.

1.5.3 The Doppler Effect

Because we focus on radiation in this paper, it is also critical to discuss relativistic effects on waves, in particular the Doppler effect. The Doppler effect is formulated under Galilean relativity to transform emitted frequencies to the observer frame. If a source with frequency f' moves toward an observer at speed u_s relative to the medium, while the observer moves toward the emitter at u_o, again relative to the medium, then the non-relativistic form of the Doppler effect specifies the observed frequency as

$$f = f' \frac{1 + u_o/v}{1 - u_s/v} \tag{1.12}$$

This fails for wave velocities at or near the speed of light, however, as their speed with respect to the medium becomes unimportant and we instead consider only the relative velocity between the source and observer, u. Radiation between the two has its frequency shifted according to the relationship

$$f = f' \sqrt{\frac{1 + u/c}{1 - u/c}} \tag{1.11}$$

For relative velocities very near c, effects are more easily differentiated by considering the Lorentz factor than its analogous relative velocity. With a velocity of $u = 0.99c$, we have $\gamma = 7.1$, but in an increase to the velocity of just 1% to $u = 0.9999c$, the Lorentz factor increases to $\gamma = 71$. For this reason, when considering highly relativistic systems, it becomes more illustrative to express the relationship in terms of the Lorentz factor instead:

$$f = (\gamma(1 - \sqrt{1 - \gamma^{-2}}))^{-1} f' \tag{1.12}$$

Chapter 2 - Methods
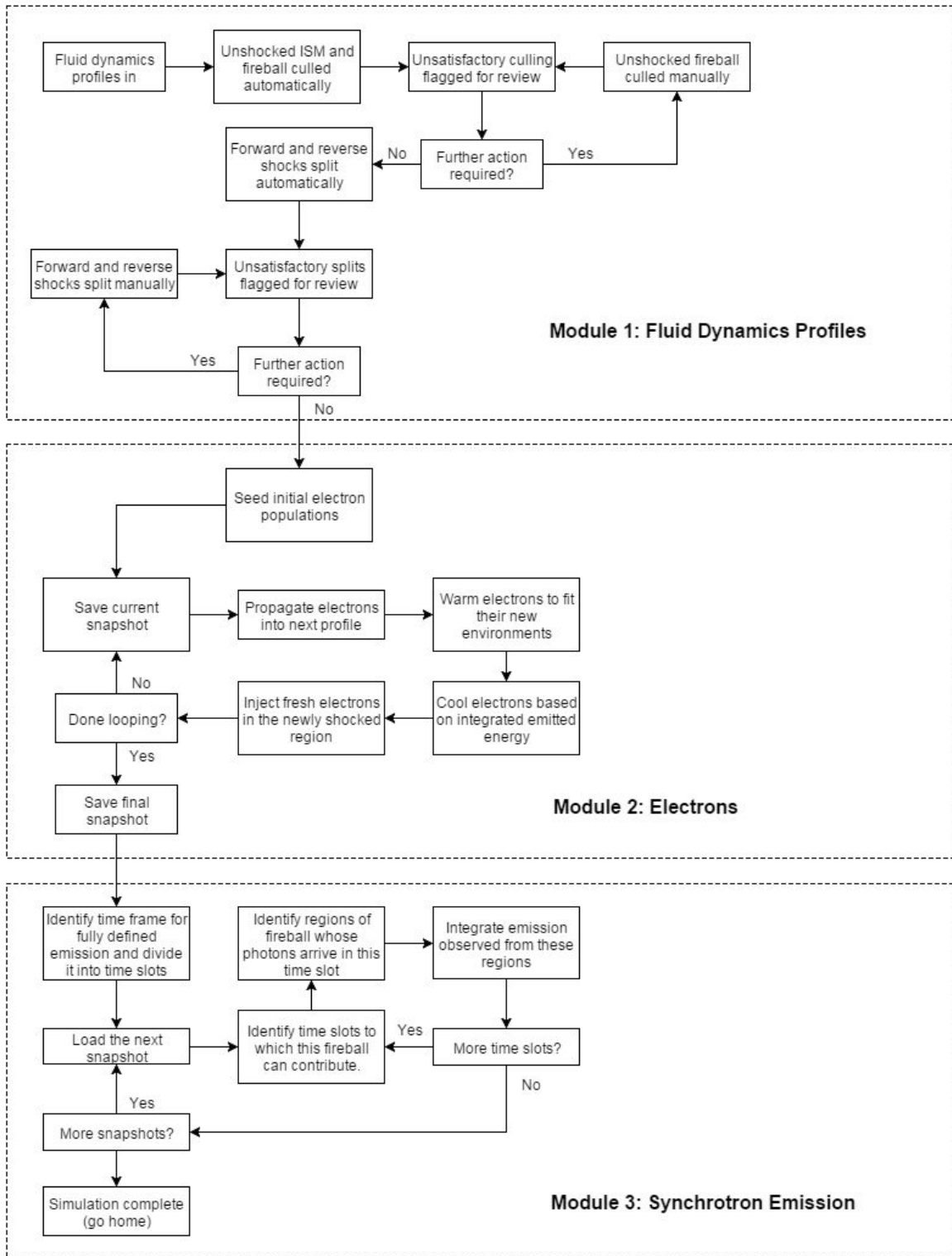
Fig 2.1. The simulation is divided into three primary modules, separately focusing on hydrodynamics, the cooling of electrons through radiation, and finally computing light curves. Highlighted are several specific methods this section will discuss in detail.

2.1 Fluid Dynamics Profiles

The outflow from which emissions are simulated is defined by three radial profiles: density, pressure, and Lorentz factor. This radial phrasing the the fluid dynamics necessarily implies the assumption of spherical symmetry in the outflow. Conceptually, this is a very poor assumption, as the theory of GRBs demands that the emission come from a collimated and ultra-relativistic jet. Functionally, however, the effects of beaming on the jet's emission are so great that for an on-axis observer, the edge behavior is wholly unobserved and the emission is indistinguishable from the isotropic model. The profiles are presented as snapshots at evenly spaced times during their evolution, which are hereafter referred to as cases. The cases were provided fully generated, and the details of their creation are beyond the scope of this paper. It can be seen in figure 2.2 that the initial density profile is characterized by three square clumps which are 100x more dense than the surrounding jet. This arrangement is chosen with the hope of producing marked features in the final light curves, but is not critical to the function of the code. With only minor adjustments for specificity, the simulation can be applied to arbitrary jet profiles.
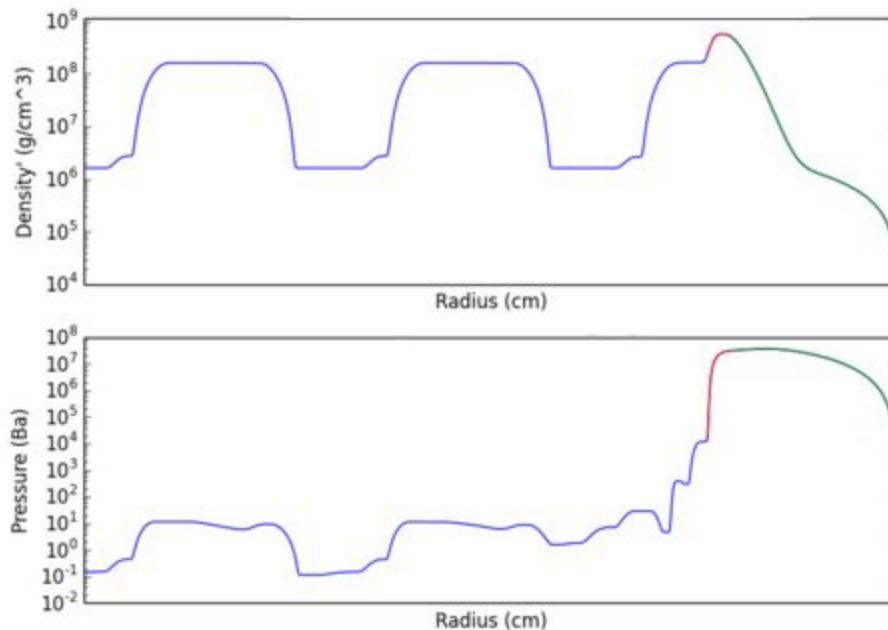

Fig 2.2. An early snapshot of the jet's radial profiles is shown, with the forward shock highlighted in green, the reverse shock in red, and the unshocked material in blue. The pictured material spans a radius of roughly 10^{11} cm.

The purpose of the fluids module is to isolate the forward and reverse shocks from the rest of the outflow. The leading edge of the reverse shock is easily distinguished from the interstellar medium by its density and pressure. The origin of the shocks is found by setting the mass in the forward shock equal to the mass of the interstellar medium which has already been swept up:

$$4\pi \int_{R}^{R-x} \rho_{jet}(r)r^2dr = \tfrac{4}{3}\pi R^3 \rho_{ISM} \qquad (2.1)$$

Where R is the radius at the front edge of the jet, ρ_{jet} is the comoving density of the jet, and x is the width of the forward shock. Finding x in this expression allows for the separation of the shocked jet material from the shocked interstellar medium. Isolating the portion of the fireball which is within the reverse shock then requires the recognition of the leading edge of the shock's retrograde motion. In a well defined case, the reverse shock's leading edge is characterized by a pressure discontinuity. Searching for these discontinuities allows for a precisely defined reverse shock front. Unfortunately, this discontinuity is not resolved for many of the provided cases, and an alternative approach is taken.

The Lorentz factor in our unshocked jet is a constant 100. For the sake of consistency, this simulation takes the point where the Lorentz factor first dips below the unshocked value to be the front of the reverse shock. Due to disturbances caused in the jet before the shock ever arrives, this criterion actually triggers well ahead of the proper shock front, and the final cut includes some unshocked jet. Fortunately for the simulation, the unshocked material contributes little to no synchrotron emissions, so the effect of its inclusion on the final light curves is negligible.

2.2 Monte Carlo Electrons

The electron module's role is to seed the fluid profiles with representative electron populations, which can later be used to quantify the synchrotron emission. This requires the creation of initial electron populations with Monte Carlo methods which are tracked as they migrate through the fireball and change energy.

2.2.1 Monte Carlo Method

Monte Carlo describes a broad class of numerical techniques unified by their use of probabilistic models. In this simulation, a set of Monte Carlo-generated electrons are taken to be representative of the radiating material in the outflow. When the simulation begins, and again whenever fresh electrons are injected at the shock front, the electrons' Lorentz factors must be initialized. A Monte Carlo approach is taken, with a power law probability density imposed. Specifically, for a uniformly random value x between 0 and 1:

$$\gamma = \gamma_0 x^{1/(p+1)} \tag{2.2}$$

In this simulation, the parameter p=-2.4 is used. The minimum Lorentz factor γ_0 is derived by considering the local temperature and converting to expected velocities for the electrons:

$$\gamma_0 = 3\frac{p+2}{p+1}\varepsilon_e P \rho^{-1}(m_e c^2)^{-1} \tag{2.3}$$

Where ε_e is the electron coupling coefficient, here taken to be 0.1, P is the local pressure, and ρ is the local comoving density.

2.2.2 Electron Migration

The electrons are initially seeded in evenly spaced clusters throughout the fireball's first case. At each step between case files, the existing electron populations are allowed to drift into position based on the local bulk Lorentz factor, as:

$$dR = c\sqrt{1-\Gamma^{-2}}dT \tag{2.4}$$

Due to the radial dependence on Γ, the electron populations propagate with different velocities within the fireball, causing them to linger in some regions and hurry through others. This trend mirrors the variations observed in the density profile of the

jet. To realize the displacement integral, time is measured in the lab frame and the intermediate bulk Lorentz factors are linearly interpolated along a grid arranged between the full length of the current case and the region of the next case which was not newly swept up. This approach occasionally sees electron clusters drift out of the region associated with the reverse shock. In these cases, the vagrant electrons are discarded and replaced with sets of new electrons in the newly shocked region.

In the majority of transitions, no electron populations drift out of the region of interest. In order to continuously inject hot electrons without causing the simulation to balloon beyond reasonable performance standards, space is made for these electrons by discarding the oldest electron clusters. Such populations have typically already cooled to the point of negligible emission, and their removal does not impact the final light curves. In some circumstances, the turbulence of the jet causes there to be little or no region associated with newly swept mass. In such cases, we simply neglect to discard and replace electron populations.

The claim of equations 2.2 and 2.3 is that the Lorentz factors depend linearly on the minimum factor, which is itself a local property. After an electron cluster drifts into a new position, its new Lorentz factors, γ', are simply warmed or cooled to reflect the new environment:

$$\gamma' = \frac{\gamma_0'}{\gamma_0}\gamma \qquad\qquad\qquad \textbf{(2.5)}$$

2.2.3 Synchrotron Cooling

The representative electrons must lose energy through radiation as time progresses. This is quantified using an equation for synchrotron power integrated over all frequencies (Ghisellini, 2012):

$$dE = \tfrac{2}{3}q_e{}^4 m_e^{-2} c^{-3} B^2 (\gamma^2 - 1)dT \qquad\qquad \textbf{(2.6)}$$

In this expression, B is taken to be the magnitude of the local magnetic field, defined by Panaitescu and Kumar (2000) as:

$$|B| = \sqrt{8\pi\varepsilon_B m_p c^2 \rho(\Gamma - 1)} \qquad\qquad \textbf{(2.7)}$$

Where ε_B is the magnetic coupling coefficient, 0.01 in this simulation, m_p is proton mass, ρ is the local comoving density of the fireball, and Γ is the local bulk Lorentz factor of the fireball. With the energy change defined, it is a simple matter to determine the change in Lorentz factor for the emitting electrons:

$$d\gamma = -\left(m_e c^2\right)^{-1} dE \qquad\qquad \textbf{(2.8)}$$

Due to the γ^2 dependence of *dE,* and consequently of $d\gamma$, the hottest electrons cool most rapidly. This has a marked effect on the distribution as time progresses, as shown in figure 2.3. There is a swift extinction of high energy electrons in the populations, which are responsible for the largest part of the synchrotron emission. This observation supports the decision to discard the oldest electron clusters.
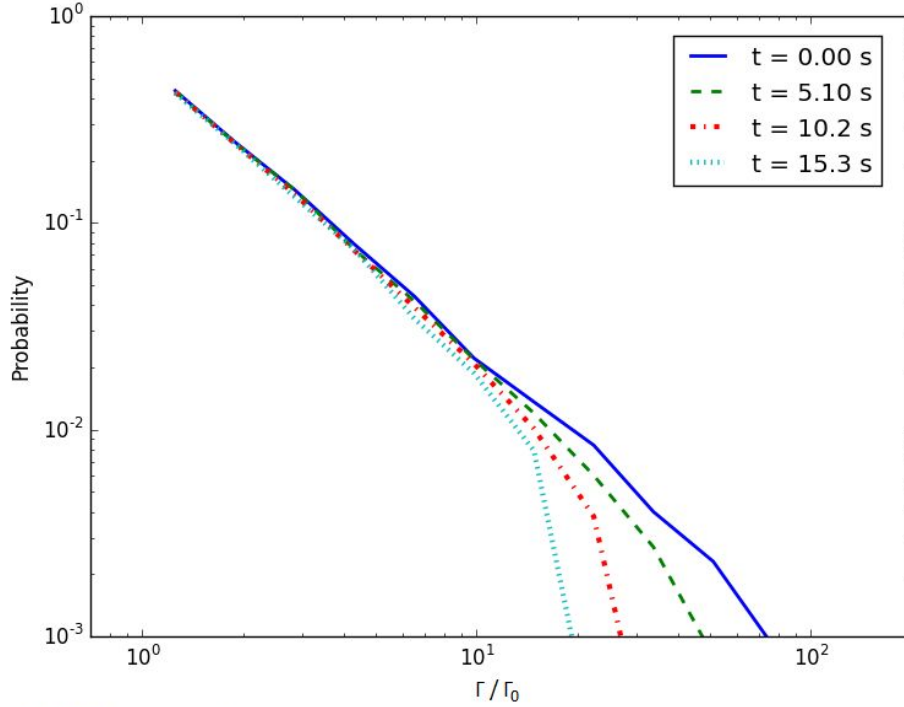
Fig 2.3. The time evolution of a stationary, example electron population is shown. It is generated with Monte Carlo methods according to a power law with p = 2.4, and resides in an arbitrary constant magnetic field of B = 130 Gauss. The most energetic electrons can be seen to go extinct, while the cooler ones are largely unaffected.

2.3 Synchrotron Emission

The emission module's purpose is to accept the fluid dynamics and electron profiles of the previous two modules, and use them to construct time-resolved spectral intensity curves. Due to the size, shape, and speed of the fireball, separating photon arrival times is non-trivial. The arrival time for an emitted photon is:

$$t_{obs} = T - Rcos(\varphi)/c \qquad (2.9)$$

where T is the emission time and (R, φ) define polar coordinates for the emission region, with the observer on the $\varphi = 0$ line. For very early or very late arrival times, some photons will have been emitted before the initial snapshot or after the last one. Because these emissions cannot be adequately quantified, observer time is restricted to times for which all incident photons must have been emitted during the snapshots. The

time range for which this is true begins with the arrival of the latest photons from the first case, and ends with the arrival of the earliest photons from the final case, or:

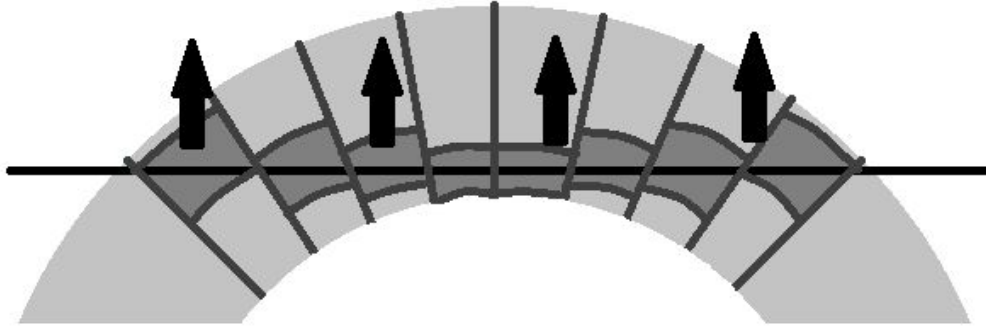$$cT_0 \leq ct_{obs} \leq cT_f - R_{f,max} \qquad \textbf{(2.10)}$$

Fig 2.4. Diagrammed is an example sectorization used when integrating a single time-slice of the fireball. For a distant observer, the photons emitted from the highlighted regions of the fireball are observed simultaneously.

Each snapshot is integrated separately. This integration is achieved by identifying which sectors of the fireball can contribute to a particular arrival time, as diagrammed in figure 2.4, where the radial bounds of the sectors are defined such that all relevant regions of the fireball will be counted once the current case's emission has been determined for all arrival times. In each sector, the density, pressure, and Lorentz factor are interpolated from the fluid profiles to calculate the average magnetic field using equation 2.7. This field is used to calculate the spectral intensity of the synchrotron emissions of the seeded electrons in the sector, and is given by Ghisellini (2012) as:

$$x = 2\pi m_e c \upsilon \left(\tfrac{3}{2}\gamma^2 q_e B\right)^{-1} \qquad \textbf{(2.11)}$$

$$I_{e,\Omega,\nu} = 3^{1/2} q_e^3 B (m_e c^2)^{-1} x \int_x^\infty K_{5/3}(y)\,dy \qquad \textbf{(2.12)}$$

Where q_e is electron charge, m_e is electron mass, υ is the emission frequency, γ is the electron's Lorentz factor, and $K_{5/3}$ is the modified Bessel function of the second type with order 5/3. The emission spectrum for a single electron is shown in figure 2.5
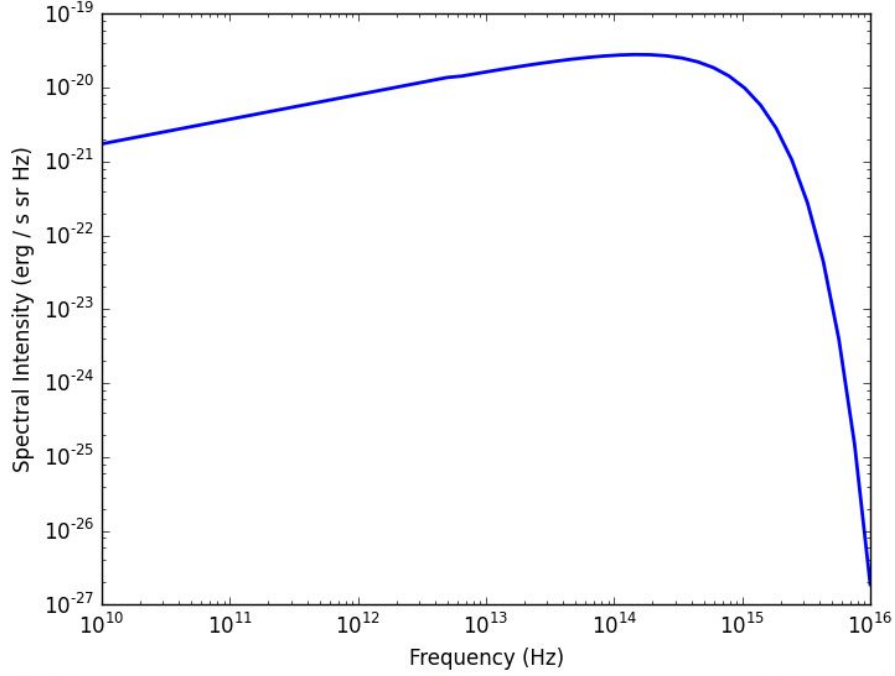
Fig 2.5. Shown is the spectral intensity due to the synchrotron emission of a single electron. This curve neglects relativistic effects between the electron and observer, and was generated with a lorentz factor of Γ = 1000 and B = 130 Gauss.

The individual electrons' contributions are taken as representative of all local electrons, and the total emission from the sector is extrapolated geometrically based on the volume and density of the sector. The spectral intensity derived this way is in the frame of the fireball; converting to the observer frame involves beaming and a Doppler shift (Rybicki, 2009).

$$v_{obs} = \left(\Gamma(1 - \sqrt{1 - \Gamma^{-2}})cos(\varphi)\right)^{-1} v_{com} \qquad \textbf{(2.13)}$$

$$I_{obs} = \left(\Gamma(1 - \sqrt{1 - \Gamma^{-2}})cos(\varphi)\right)^{-4} I_{com} \qquad \textbf{(2.14)}$$

In these equations, Γ is the local bulk Lorentz factor, and φ is the mean polar angle of the sector. Integrating the emissions over the time between cases, the duration of emission is similarly affected by a Doppler factor.

$$T_{obs} = (\Gamma(1 - \sqrt{1 - \Gamma^{-2}})cos(\varphi)) \, T_{com} \tag{2.15}$$

Considering the geometry of the fireball and relativistic effects, the synchrotron emissions during the valid time range are integrated from the case files.

Chapter 3 - Results and Discussion

3.1 Calibration Curve

The simulation's early bugs were corrected by computing observer frame light curves for a well understood model, the Blandford-McKee (BM) solution for spherically symmetric, relativistic shocks. Their paper provided analytical and simple hydrodynamics in which electrons were seeded and curves computed. Many theoretical light curves have been computed for the BM model, and we adopt the solution of Panaitescu and Kumar (PK) for comparison in figure 3.1. The PK solution gives a broken power law for the fading face of the light curve,

$$\text{Uncooled: } I_v = 10^{2.4-0.8p} E^{(p+3)/4} n_*^{1/2} \varepsilon_e^{p-1} \varepsilon_B^{(p+1)/4} v^{-(p-1)/2} T^{(3/4)(p-1)} \tag{3.1}$$

$$\text{Cooled: } I_v = 10^{2.4-0.8p} E^{(p+2)/4} \varepsilon_e^{p-1} \varepsilon_B^{(p-2)/4} v^{-(p/2)} T^{-(3p-2)/4} \tag{3.2}$$

Where p is the slope of the electron Lorentz factor power law, E is the total isotropic energy of the burst, ε_e and ε_B are energy coupling coefficients for the electric and magnetic fields, v is the frequency, and T is the time since the first photon's arrival. The intersection of the two lines marks what is known as the cooling break. This appears once the synchrotron cooling, which is fastest for the hottest electrons, has bent all the individual spectra to peak below the frequency of interest.
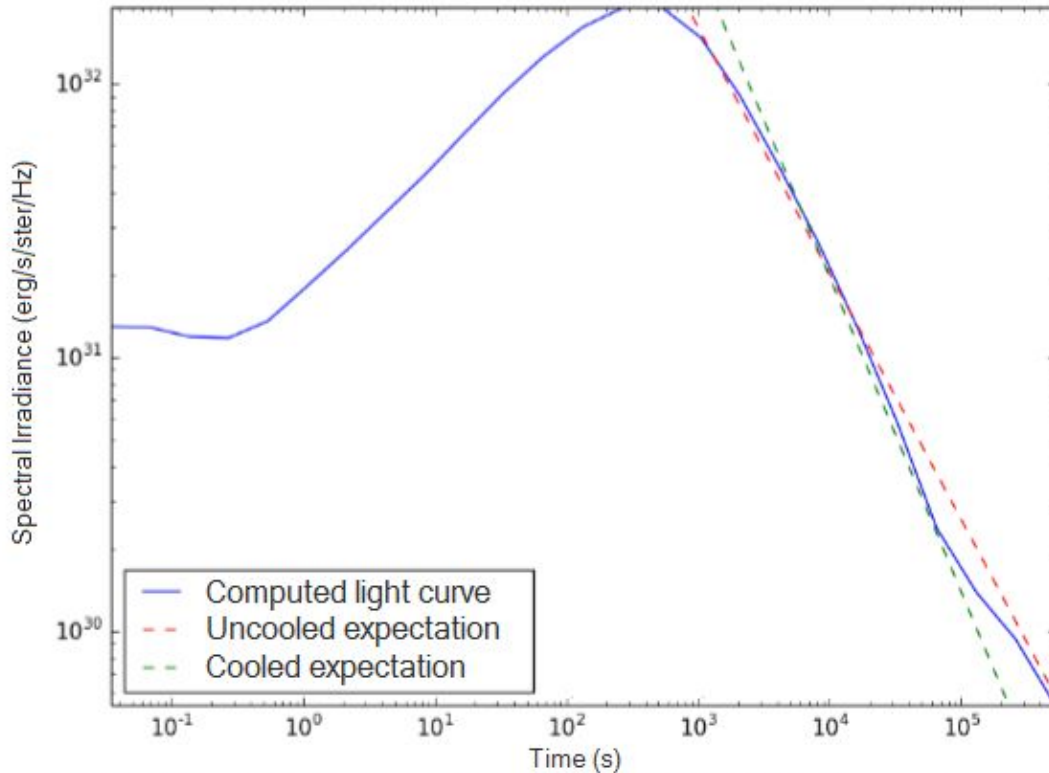
Fig. 3.1 The simulation was tested with Blandford McKee hydrodynamics. The blue curve indicates the synchrotron produced, while the dashed lines denote two regimes in the broken power law of Panaitescu and Kumar's analytical solution.

The produced curve ramps smoothly to a peak before fading away, and closely matches the PK prediction for the uncooled regime for times of roughly 10^3 s to 10^4 s. It bends downward at the cooling break to match the prediction for the cooled regime from 10^4 s to roughly 7×10^4 s, but flares unexpectedly in the final moments of the simulation. With Monte Carlo style simulations, noise can be reduced by increasing the number of representative individuals in a population. The flare occurs at a time when the signal is minimal, which is to say that the number of sample electrons contributing to that irradiance is small. With this in mind, we interpret that flare as just noise in the simulation. This code is was written to act on a forward shock, so some adjustments were made to reach the final state of the simulation. The changes were small and obvious, however, so we consider this result to be a validation of the physics used in the final version of the simulation.

3.2 Light Curves

The full suite of the simulation was applied to GRB hydrodynamics profiles featuring three dense shells of thickness and separation on the order of 10^{10} cm. We calculated observer frame light curves for frequencies ranging from the radio band to gamma rays, but select 600 nm red, 60 nm UV, and x rays at 6 nm and 0.6 nm for display in figure 3.2.
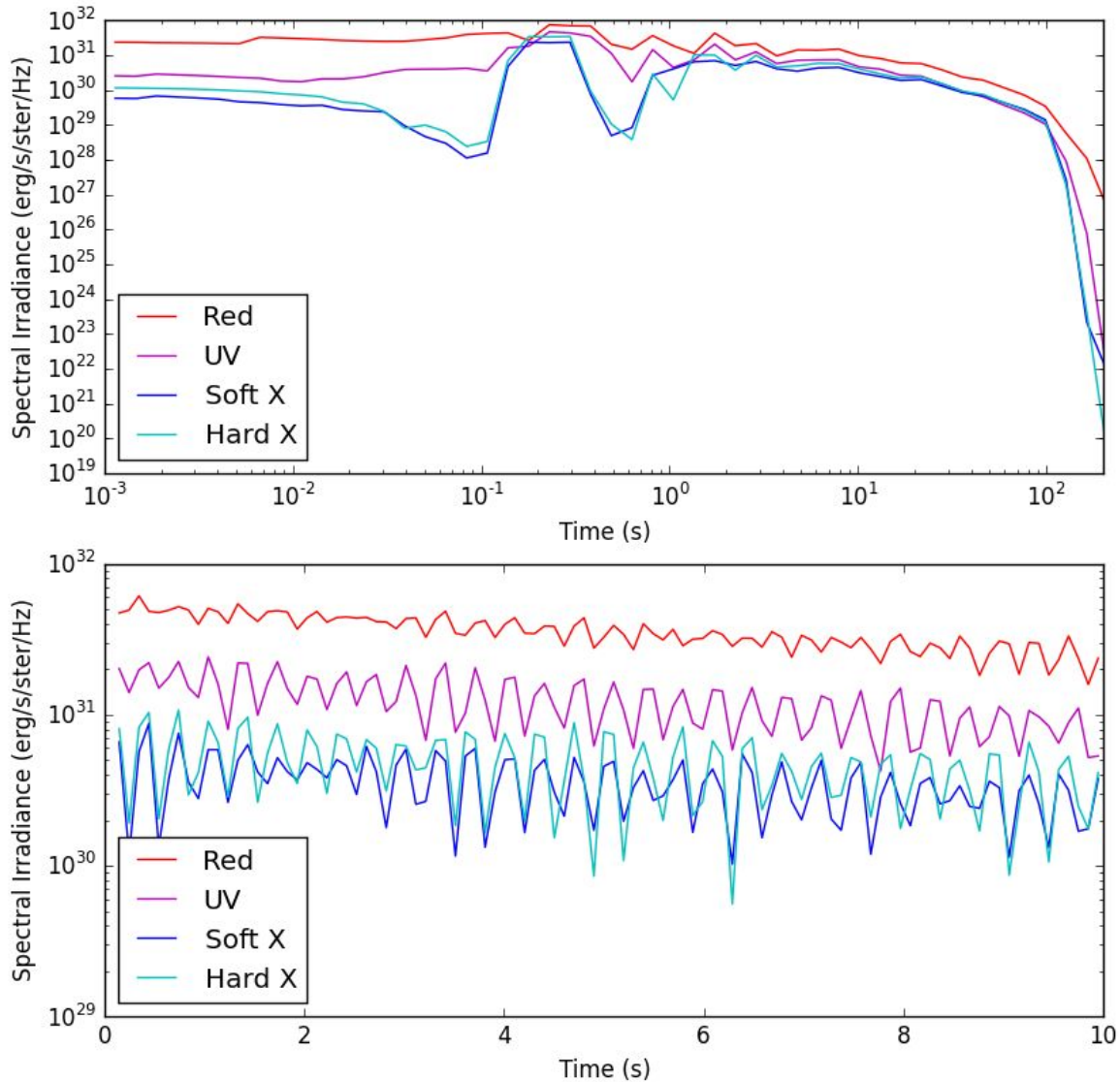
Fig. 3.2 Shown are light curves calculated at wavelengths 600 nm (red), 60 nm (UV), 6 nm (soft X rays), and 0.6 nm (hard X rays). The upper plot shows the full duration of the flash, while the lower plot highlights the time frame where the jet geometry is expected to produce variability.

The full light curves produced with the GRB hydrodynamics show no evidence of the ramping up seen in figure 3.1. The synchrotron irradiance observed at all frequencies begins a sharp decline near 100 s, but is nearly constant, decreasing only slightly before the cutoff. This constant irradiance is greater for lower frequencies, with the highest shown belonging to optical light. The irradiance continues to increase through infrared and into radio, before decreasing again below 10^{10} Hz. A deviation from this trend is shown in figure 3.2, with hard x rays being slightly brighter than their soft counterparts for most of the flash's duration.

The full curves suggest high variability between the times 10^{-2} s and 10 s, but further calculations on that interval with finer integration parameters eliminated the behavior rather than highlighting it. The curves computed for the GRB reverse shock also exhibit much greater noise than the calibration curve, despite receiving hours and days longer computation from tightened integration parameters.

3.3   Comparison to Expectations

To validate the computed light curves, we compare them to the optical flash predictions of Kobayashi. Under the conditions for our jet and the the frequencies we are interested in, his equations reduce to a constant intensity for times before the shock has fully crossed the shell ($t < T$), and 0 after. The constant intensity is given by

$$I_v = 0.3\varepsilon_B^{1/2}E^{5/4}n_1^{1/4}\eta^{-1}T^{-3/4} \tag{3.3}$$

Where the new parameters η and n_1 represent the bulk Lorentz factor of the shell and the density of the ISM, respectively. The computed red and UV curves are shown against Kobayashi's predictions in figure 3.3

24
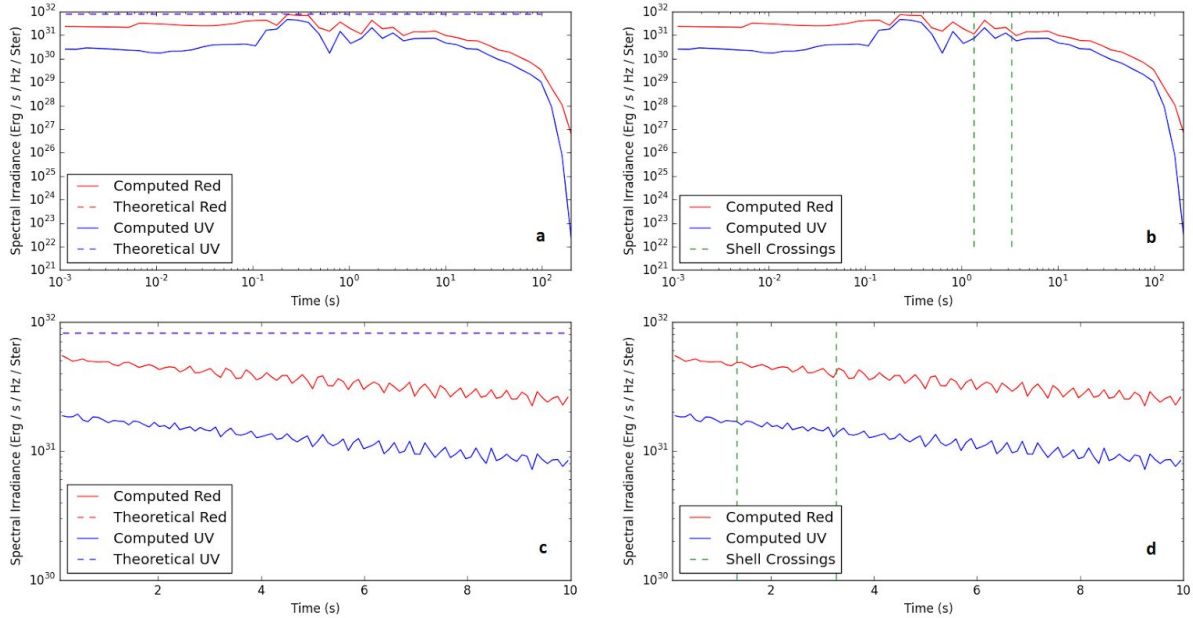
Fig 3.3 Subplots **a** and **b** show the light curves for 600 nm red and 60 nm UV against the prediction of Kobayashi. The red curve stays within a factor of 2 during the highlighted interval, while the UV curve stays within an order of magnitude. Both curves remain below the predicted irradiance for the full duration. In **a**, the cutoff in Kobayashi's prediction coincides with the cutoff for our curves. Subplots **b** and **d** identify the times at which the geometry of our jet suggests that there will be enhanced emission.

Kobayashi's predictions agree well with our own curves. While the analytical model calls for consistently greater irradiance than the simulation produced, there is a critical difference between the two sources. The prediction requires the assumption of a single thick shell, while the simulation acts on three thinner shells spaced through the same radii. The thick shell assumption gives the prediction nearly double the amount of shocked matter, so it is within reason that it would produce twice the radiation of the optical curve.

Figure 3.3 also highlights a failing in the simulation, however. As the shock front reaches the second and third shell at observer times 1.35 s and 2.37 s, respectively, we expect the sharp increase in the availability of shocked material to produce a surge in radiation to irradiances at least as large as the initial values. While the lower resolution, full duration curve might suggest such an effect, finer inspection of the interval showed a simple decreasing trend. The noise in 3.3d is low enough to discount any alternate interpretation.

3.4 Error Analysis

The signal's lack of response to the variability in the jet represents a serious failure in the simulation. The absence of an initial increasing phase in the light curves is problematic as well, though the two are likely to share a cause. Further testing of the simulation is underway to identify the root of the error, and hopefully identify a solution. The emission module is being applied to a linearly growing body of electrons which do not cool. If the resultant light curve has the expected increasing trend, then the hydrodynamics processing and electron seeding modules will be implicated as the point of failure. If the test curve is constant or decreasing, then we will know that the error lies within the emission module.

If the first two models are found to contain the error, there is one principle assumption which may be responsible. We question the belief that the unshocked jet included within the region designated as reverse shock does not contribute significant radiation. Due to the gentler conditions, the electrons in that region would have a synchrotron spectrum peaking at lower frequencies. If they radiate a significant portion of their energy away before being shocked, then our expectation of enhanced emission would be dampened by the premature cooling of those electrons. This could be tested by computing curves with and without the unshocked material for cases where the reverse shock front is easily identified, and by determining Lorentz factor distributions for prematurely cooled electron populations. The effects of cooling on this distribution is shown in figure 2.3, where the loss of the hottest electrons might prevent enhanced emission in the optical band. Fixing this issue would pose a significant challenge, as the assumption was originally only taken for lack of a better solution.

The emission module is virtually unchanged from the version which produced the strong agreement with theory shown in figure 4.1. If the test case identifies it as the root of the problem, then it would most likely be a simple coding mistake. The alterations necessary on this module were very few, strictly limiting the potential locations of the error. If this module contains the mistake, it would likely be an easy fix. It remains a

possibility that the error was present during the calibration curve, but given the quality of the fit, we find this extremely unlikely.

<u>Chapter 4 - Conclusion</u>

The discovery of gamma ray bursts in the 1970s woke the world's astronomers to a new spectrum of observational possibilities, and launched an exciting new branch of astrophysics. Recent technological advances have made it clear that the mysterious optical flashes associated with GRBs are much more common than once thought. The most commonly accepted models hold that these flashes are the product of synchrotron radiation in the reverse shock of a GRB's jet.

Through the construction of a Monte Carlo style simulation, we have demonstrated that this mechanism is fully capable of producing optical flashes in the magnitudes and durations observed. Furthermore, this is achieved using a highly variable three-shell jet, which would be impossible to solve analytically. The nature of our outflow indicates a flaw somewhere in the simulation, however, as we do not resolve any variation in the light curves associated with the internal geometry of the jet. This poses a question to the validity of the simulation, though we hold that its results are still broadly correct. Further work with the code is underway to identify and solve this bug.

Assuming that the simulation is fixed, it presents several opportunities for future research. Particularly interesting to me is the idea of fitting hydrodynamics to burst observations. If the geometry of the jet can be reflected in its light curves, then it may be possible to construct and tailor a jet to emit radiation that matches light curves which have been measured from real GRBs. This would provide insight into the local conditions from which the burst originated, including properties of the ISM, progenitor star, and the central engine. The code could also be incorporated into a larger simulation for the whole range of emission from a GRB, including the prompt gamma and the afterglow. Before either of these projects could be undertaken in earnest, however, it may prove necessary to optimize the code.

Acknowledgements

Bibliography

1. Ghisellini, G. "Radiative Processes in High Energy Astrophysics." Springer International Publishing, 2012.
2. Gehrels, N., Ramirez-Ruiz, E., and Fox, D.B. "Gamma-Ray Bursts in the Swift Era." *Annual Review of Astronomy and Astrophysics* **47**, 567-617. 2009.
3. Meszaros, P. "Theories of Gamma-Ray Bursts." *Annual Review of Astronomy and Astrophysics* **40**, 137-169. 2002.
4. Sari, R. and Piran, T. "Predictions for the very early afterglow and the optical flash." *The Astrophysical Journal* **520**, 641-649. 1999.
5. Rybicki and Lightman. *Radiative Processes in Astrophysics*. Wiley: New York, 1979.
6. Panaitescu A. and Kumar, P. "Analytic Light Curves of Gamma-Ray Burst Afterglows: Homogeneous Versus Wind External Media." *The Astrophysical Journal* **543**, 66-76. 2000.
7. Blandford, R. and McKee, C. "Fluid dynamics of relativistic blast waves." *Physics of Fluids* **19**. 1130. 1976.

Appendix A - Other Light Curves